

Geophysical Research Letters

RESEARCH LETTER

10.1029/2019GL085888

Key Points:

- We use earthquake waveform similarity as a tool to study how stress and faulting evolve during the Ridgecrest sequence
- Ridgecrest aftershocks have lower similarity than pre-event seismicity, implying stress and fault heterogeneity at 100-m length scales
- Ridgecrest aftershocks show coherent spatial variations in similarity that correlate with along-strike variations in mainshock fault slip

Supporting Information:

- Supporting Information S1
- Data Set S1

Correspondence to:

D. T. Trugman,
dtrugman@lanl.gov

Citation:

Trugman, D. T., Ross, Z. E., & Johnson, P. A. (2020). Imaging stress and faulting complexity through earthquake waveform similarity. *Geophysical Research Letters*, 47, e2019GL085888. <https://doi.org/10.1029/2019GL085888>

Received 17 OCT 2019

Accepted 23 DEC 2019

Accepted article online 3 JAN 2020

Imaging Stress and Faulting Complexity Through Earthquake Waveform Similarity

Daniel T. Trugman¹, Zachary E. Ross², and Paul A. Johnson¹

¹Geophysics Group, Earth and Environmental Sciences Division, Los Alamos National Laboratory, Los Alamos, NM, USA, ²Seismological Laboratory, California Institute of Technology, Pasadena, CA, USA

Abstract While the rupture processes of nearby earthquakes are often highly similar, characterizing the differences can provide insight into the complexity of the stress field and fault network in which the earthquakes occur. Here we perform a comprehensive analysis of earthquake waveform similarity to characterize rupture processes in the vicinity of Ridgecrest, California. We quantify how similar each earthquake is to neighboring events through cross correlation of full waveforms. The July 2019 Ridgecrest mainshocks impose a step reduction in earthquake similarity, which suggests variability in the residual stress field and activated fault structures on length scales of hundreds of meters or less. Among these aftershocks, we observe coherent spatial variations of earthquake similarity along the mainshock rupture trace, and document antisimilar aftershock pairs with waveforms that are nearly identical but with reversed polarity. These observations provide new, high-resolution constraints on stress transfer and faulting complexity throughout the Ridgecrest earthquake sequence.

Plain Language Summary Earthquakes that occur nearby to one another typically broadcast similar seismic signals. In this work, we show that the $M6.4$ and $M7.1$ earthquakes that occurred as part of July 2019 Ridgecrest, California, earthquake sequence triggered measurable changes in the similarity of earthquake waveforms throughout the nearby region. This implies high levels of complexity in the crustal stress field and active fault structures on the scale of tens to hundreds of meters. The Ridgecrest mainshocks caused earthquakes to become less similar on average, with systematic spatial variations along the rupture planes in correspondence to the level of mainshock fault slip. These observations form the basis for future work relating measurements of earthquake similarity to changes in stress and strength in Earth's crust.

1. Introduction

Underlying all earthquake processes is a balance of stress and strength. Because of this, a detailed characterization of the crustal stress field and fault mechanical properties is fundamental to the physics of earthquake triggering. To understand how and why earthquakes nucleate, rupture, and arrest, we need better observational constraints on the stresses that trigger earthquakes to initiate, as well as the fault systems that provide mechanical weaknesses and pathways for ruptures to evolve. Despite this importance, few techniques exist to image stresses and faults in high resolution. In this work, we use careful measurements of earthquake waveform similarity to examine how stress and faulting complexity evolves in response to a large earthquake, with observations from the recent Ridgecrest, California, earthquake sequence as our guide.

On 4 July 2019, a $M6.4$ earthquake struck a remote area of the Eastern California Shear Zone near Ridgecrest, California, north of the Garlock fault and slightly east of the Little Lake Fault system. The $M6.4$ earthquake was followed less than 34 hr later by a $M7.1$ earthquake that ruptured a 75-km-long, nearly orthogonal fault system. This cross-fault triggering mechanism is reminiscent of the 1987 Superstition Hills sequence in Southern California, and both the left-lateral $M6.4$ and right-lateral $M7.1$ events were preceded by notable foreshock sequences and vigorously triggered aftershocks at local and more remote distances (Barnhart et al., 2019; Liu et al., 2019; Ross et al., 2019). The impact of these earthquakes was limited by their distance from major population centers, though strong shaking was observed locally in the towns of Ridgecrest and Trona, among others, and the surface rupture penetrated the Naval Air Weapons Station at China Lake.

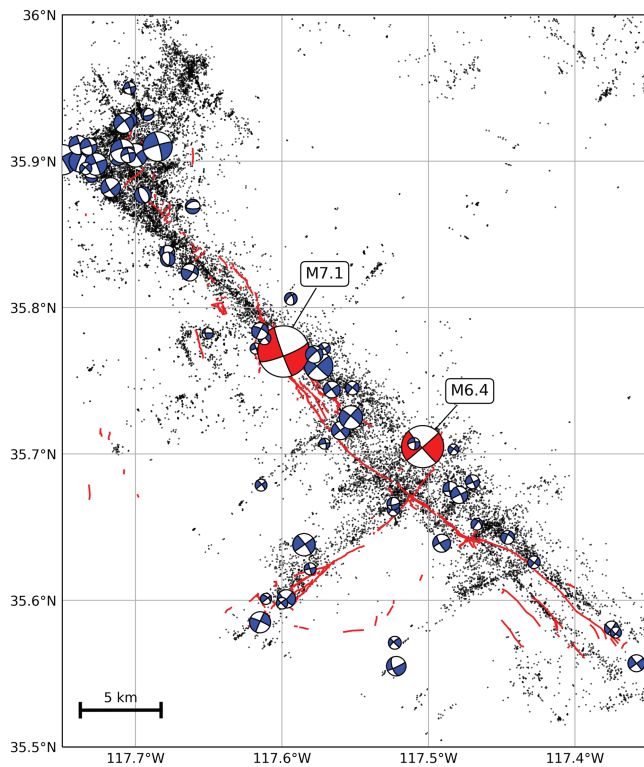


Figure 1. Map of the study region. Relocated earthquakes from 1 January 2000 to 28 August 2019 are shown as black dots. Focal mechanism estimates for magnitude $M4$ and $M5$ earthquakes are shown in blue, with the $M6.4$ and $M7.1$ mainshocks shown in red. Field-verified locations of surface rupture are marked with red lines.

The Ridgecrest earthquake sequence provides a rich dataset to study several different aspects of earthquake occurrence. Our focus here is on using measurements of earthquake similarity to probe spatiotemporal changes in the crustal stress distribution and fault network. To do this, we perform a comprehensive analysis of waveform similarity near Ridgecrest California from 1 January 2000 to 28 August 2019, a time period which includes nearly 20 years of background, pre-event seismicity, and 8 weeks of post-event aftershocks. We measure waveform similarity for each earthquake by crosscorrelating the full waveforms of each event with those of other earthquakes occurring nearby in space. By averaging across stations and neighboring events, these waveform similarity coefficients provide a direct and quantitative measure of how similar each earthquake is to other nearby events. We validate this waveform-based approach by examining rotations in earthquake focal mechanisms, which provide an alternative measure of earthquake similarity, though at coarser resolution.

The July 2019 Ridgecrest mainshocks have a marked impact on earthquake similarity in this region. We observe a step decrease in earthquake similarity that is closely aligned with the initiation of this sequence. The Ridgecrest aftershocks exhibit spatial variations in earthquake similarity, with particularly low values within a high slip patch near the $M7.1$ hypocenter. We also observe repeated instances of antisimilar earthquakes among the Ridgecrest aftershocks, with waveforms with reversed polarity that suggest a complete reversal in fault slip over a short length scale. Taken as a whole, our results show that large earthquakes like those of the 2019 Ridgecrest sequence can imprint highly complex residual stress fields replete with a diverse mesh of active faulting structures.

2. Data and Methodology

We focus on seismicity from 1 January 2000 to 28 August 2019 within a geographic region surrounding the July 2019 Ridgecrest rupture complex (Figure 1 and Figure S1 in the supporting information), with longitude and latitude boundaries of $[-117.75^\circ, -117.35^\circ]$ and $[35.50^\circ, 36.00^\circ]$. This study area encompasses the fault traces of both the $M6.4$ and $M7.1$ events but cuts off to the southeast of Coso Geothermal Field and to the north of the Garlock Fault. We use three main data sets in this study: (1) initial earthquake locations and phase arrival estimates, (2) triggered waveforms from local broadband and short-period (HH and EH code) stations within 80-km epicentral distance, and (3) focal mechanism estimates derived from P wave first motion and S/P amplitude ratio data (Hardebeck & Shearer, 2003; Yang et al., 2012). All three data sets are publicly available from the Southern California Earthquake Data Center (<https://scedc.caltech.edu>).

As a preliminary step in our analyses, we refine the precision of the input earthquake hypocenters using relative relocation techniques. For each earthquake in our study region, we select 1.5-s-long P wave and S wave windows at stations within 80-km epicentral distance using manually reviewed SCSN analyst picks where available and supplementing these picks with theoretical arrivals computed from the 1-D velocity model of Hauksson and Unruh (2007). We then cross-correlate waveforms from each event with its 300 nearest neighbors to obtain differential travel time estimates at common stations. We subset this differential travel time data set to include only results with peak cross-correlation values greater than 0.7 and use the relative relocation algorithm GrowClust (Trugman & Shearer, 2017) to refine the hypocentral locations. In total, we relocate 27,005 earthquakes in our study region (84% of the 32,246 listed in the SCSN catalog) and perform bootstrap resampling to estimate median horizontal and vertical uncertainties of 57 and 127 m.

With the relocated catalog in hand, we next endeavor to measure the waveform similarity of each earthquake with nearby events. To do this, we again cross-correlate pairs of earthquakes in close spatial proximity, this time using the full waveform, including both P and S arrivals, as well as their coda. For each station recording an earthquake, we define a distance-dependent time window designed to enclose both the P wave and S

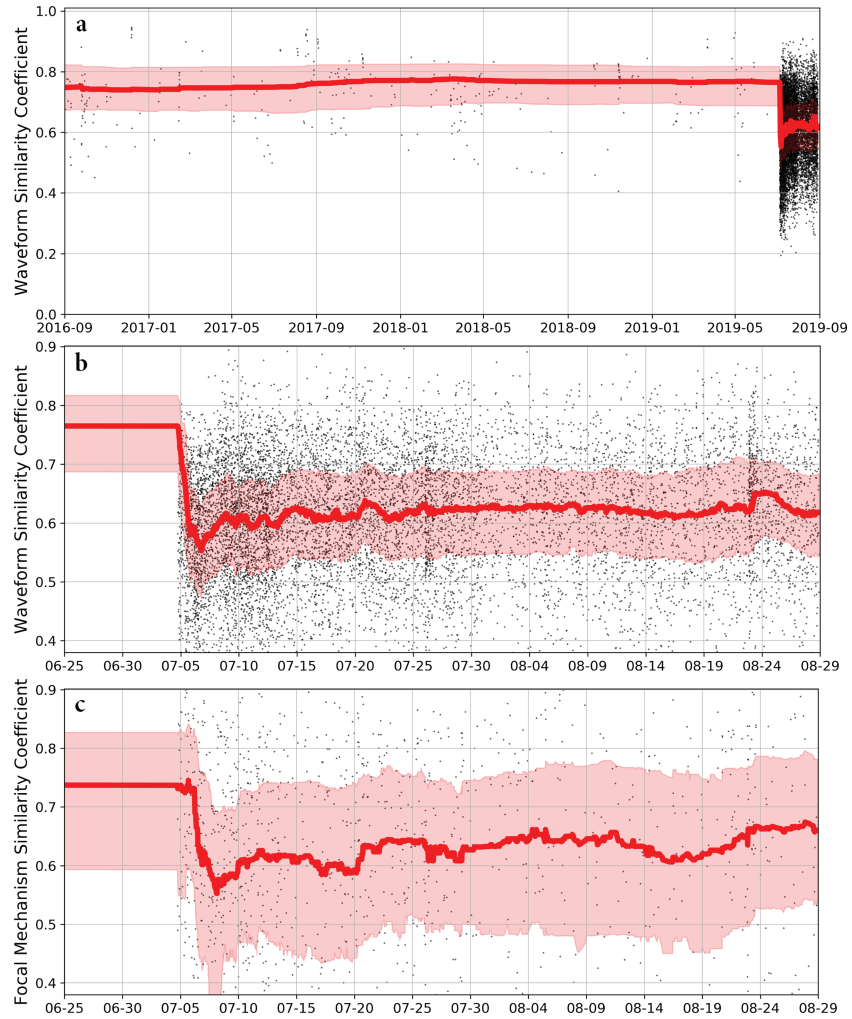


Figure 2. Time series of waveform and focal mechanism similarity coefficients. Each panel shows measurements of individual earthquakes as black dots, median values from causal, 400-event moving windows as solid red lines, and the interquartile range of these windows as shaded envelopes. Panel (a) shows the time evolution of waveform similarity coefficients SW in the 3 years preceding the July 2019 Ridgecrest sequence. Panels (b) and (c) zoom in on the sequence itself, plotting the time evolution of waveform similarity SW and focal mechanism similarity SF , respectively. The uncertainties and spread in observations are notably larger for the mechanism-based estimates in (c) than for the waveform-based estimates in (b).

wave without extending too far into the post-event noise, which could bias cross-correlation estimates. We begin this window 0.5 s before the P wave arrival and end it at a time $T_{postS} = 3.0 + 0.1R$ s after the predicted S arrival, where R is the epicentral distance in kilometers. These values were selected by visually inspecting waveforms to ensure that the dominant portion of the signal was captured at epicentral distances from 0 to 80 km. We band-pass filter all waveforms from 1–12 Hz and use a GPU-based frequency domain code to rapidly cross correlate all relocated events with nearby earthquakes. We save peak cross-correlation results for all stations that meet a minimum signal-to-noise ratio criteria, instead of only values exceeding a predefined threshold of use for earthquake location (e.g., 0.7 as used in the relocation step above).

For each earthquake i , we define waveform similarity coefficient SW_i as the average cross correlation CC with all neighboring earthquakes j within a fixed hypocentral distance RH_{max} :

$$SW_i = \frac{1}{N_{neigh}} \sum_{j=1}^{N_{neigh}} \left[\frac{1}{N_{sta}} \sum_{k=1}^{N_{sta}} CC_{ij;k} \right]. \quad (1)$$

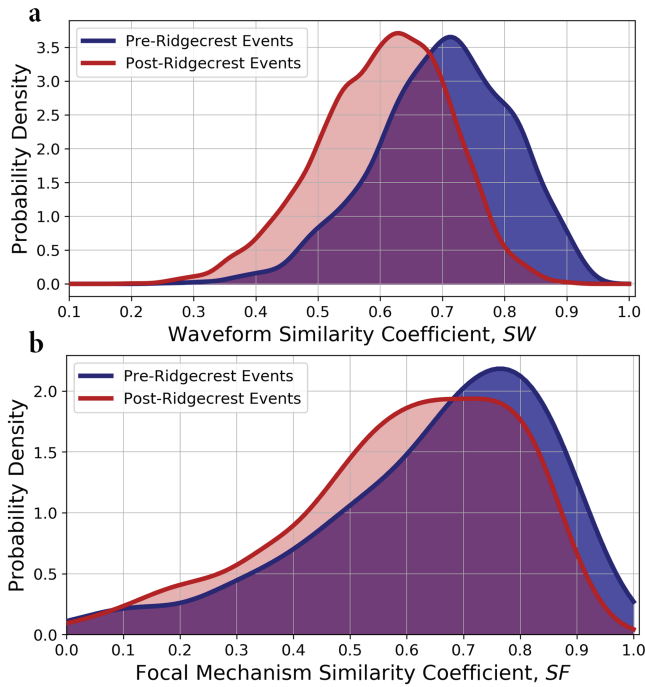


Figure 3. Temporal changes in the distribution of waveform and focal mechanism similarity coefficients. Panels (a) and (b), respectively, show kernel density estimates of the probability distributions for waveform similarity SW and focal mechanism similarity SF , each normalized to integrate to one. The pre-event and post-event distributions are, respectively, colored in blue and red, with individual event estimates denoted as small black circles.

For the results presented in this paper, we set RH_{max} to a close value of 300 m with an aim to ensure that neighboring events should have comparable Green's functions within the frequency band of interest. To improve robustness, we only consider event pairs with at least three mutual stations and only compute SW values for events with at least three neighbors within RH_{max} . Since large earthquakes can induce local changes in the Green's functions due to off-fault damage (Cochran et al., 2009; Mitchell & Faulkner, 2009), we temporally partition the data set at the start of the July 2019 sequence. In this way, two earthquakes are only considered neighbors if they either both occur before or both occur after the Ridgecrest mainshocks, a condition that helps ensure that neighbors have comparable Green's functions. The central results of this study turn out not to be very sensitive to RH_{max} and other parameter choices (Figures S2 and S3) or to the temporal partitioning (Figure S4). We also find that there is a negligible correlation between spatial event density and waveform similarity ($r^2 \sim 0.01$, explaining 1% of the variance), which is a useful check that our primary observations are not controlled by the tendency for increased clustering in aftershock sequences compared to pre-event seismicity. Finally, for each earthquake, we estimate uncertainties in SW_i by applying bootstrap resampling to the input cross-correlation data, with typical values of order 0.05 in normalized cross-correlation units.

For the purposes of comparison with the waveform similarity metric, we also measure the similarity in the focal mechanisms of nearby earthquakes. Here, we use a high-quality subset of the full SCSN focal mechanism catalog, restricting our analyses to only those events with A or B quality focal mechanisms. For each pair of mechanisms, we then use a quaternion formulation (Kagan, 2013) to compute the minimum rotation angle ϕ_{ij} needed to align the two mechanisms, an approach that elegantly avoids potential issues related to nodal plane ambiguity. We then calculate an analogous mechanism similarity coefficient based on the average rotation ϕ needed to align event i with its neighbors:

$$SF_i = \frac{1}{N_{neigh}} \sum_{j=1}^{N_{neigh}} \frac{90 - \phi_{ij}}{90}, \quad (2)$$

where ϕ is measured in degrees. Note that higher values of the average rotation angle ϕ indicate lower levels of similarity, so the SF coefficients are transformed as above so that they reflect a measure of similarity, not dissimilarity. For these focal mechanism similarity calculations, we require only two neighboring events (instead of three) within 300-m hypocentral distance due to the relative scarcity of quality mechanism estimates.

3. Results

The initiation of the July 2019 Ridgecrest earthquake sequence denotes a clear temporal demarcation in earthquake rupture similarity within our study region. We assess this in two ways: first by computing the median similarity coefficient as a function of time using causal windows of 400 events ending at each event origin time, and second by comparing probability distributions of similarity coefficients before and after the start of the July 2019 sequence. We observe a distinct drop in median similarity as the sequence commences, one which does not recover to pre-event values during our 8-week sample of the aftershock sequence (Figure 2). This temporal change in rupture similarity suggests a complex residual stress field in the aftermath of the Ridgecrest mainshocks, as the pre-event seismicity does not exhibit any comparable change. A comparison of the distribution of earthquake similarity coefficients for earthquakes before and after the sequence begins (Figure 3) confirms these results. Earthquakes occurring from Year 2000 to 3 July 2019 tend to be highly similar, while the aftershocks from 4 July and onward exhibit lower similarity values. The widths of the pre-event and post-event distributions appear roughly constant.

We also observe clear spatial variations in similarity among the aftershocks of the July 2019 Ridgecrest earthquake sequence. Earthquakes in the hypocentral region of the $M7.1$ (near -117.605° , 35.766°) tend to have

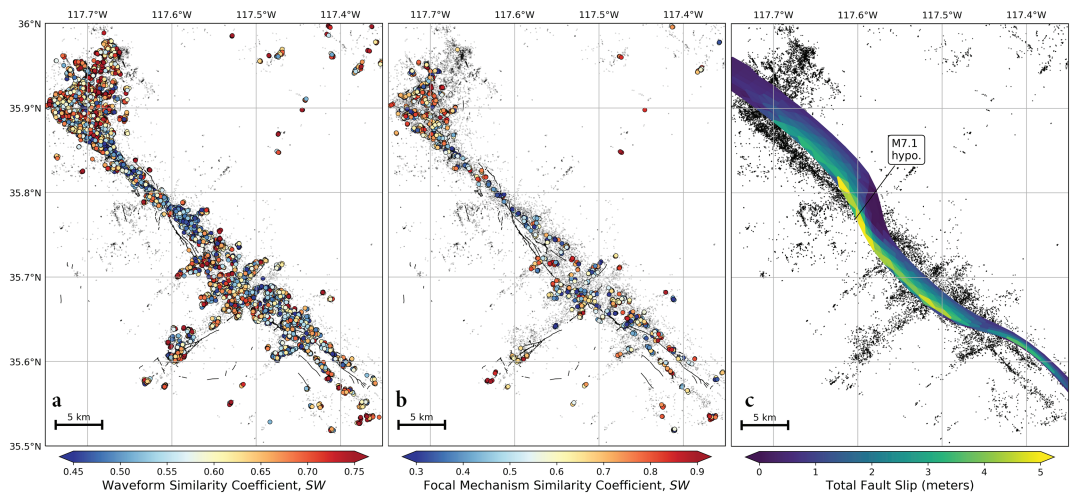


Figure 4. Map view picture of waveform and focal mechanism similarity coefficients of the Ridgecrest aftershock sequence and their relation to mainshock fault slip. Panels (a) and (b), respectively, show locations for events with valid waveform similarity SW and focal mechanism similarity SF estimates, with values color coded such that warmer colors indicate higher levels of similarity. Note that valid measurements of SF are sparse compared to those of SW due to a relative lack of densely distributed and high-quality mechanism estimates. Panel (c) shows the total slip distribution of the $M7.1$ mainshock from the static inversion of Barnhart et al. (2019).

markedly lower similarity values than events in other regions (Figure 4). This location is particularly notable because it is the portion of the rupture with the highest slip (e.g., Barnhart et al., 2019), which suggests a correspondence between earthquake similarity and the degree of heterogeneity in the residual stress field. In contrast, the events near the northwestern rupture terminus are characterized by high similarity, suggesting a relatively homogeneous stress field and a uniform set of faulting structures. Some of the other, more isolated structures away from the main fault trace also show high similarity values. Because there is little spatial overlap between events occurring before and after the start of the July 2019 sequence (Figure S5), we cannot completely rule out the contribution of a change in earthquake location to the observed temporal trend. However, a simple change in earthquake locations without large-scale perturbations in stress or strength is unlikely to explain the observations in full, as similarity values are quite stable in the preceding 20 years despite shifts in earthquake sequence locations all across the study region.

The overall tendency for low waveform similarity among the Ridgecrest aftershocks is perhaps best exemplified by the occurrence of nearby earthquake pairs with antisimilar waveforms that are nearly identical but reversed in their polarity (Figures 5 and S6). Waveforms from these earthquake pairs have sharply peaked but strongly negative cross-correlation functions at multiple stations. If we define an antisimilar earthquake pair to have peak negative cross-correlation values of -0.85 or less at five or more stations, we document 45 such instances among the Ridgecrest aftershocks. These antisimilar earthquake pairs tend to occur on adjacent but not overlapping fault patches (with typical interevent distances of several hundreds of meters) and in the central part of the rupture zone (Figure S7), where lower median levels of waveform similarity are observed. We do not observe any instance of antisimilar earthquake pairs among the pre-event seismicity, so their occurrence appears to be limited to the aftershock sequence. It is worth noting that the occurrence of antisimilarity is still quite rare within our data set on a percentage basis, which implies that it is not a pervasive phenomenon comparable to the tidally driven slip reversals of deep moonquakes (Frohlich & Nakamura, 2009). However, these observations confirm the initial findings of Ma and Wu (2013) of a small number of antisimilar waveforms among the aftershocks of the 2008 $M7.9$ Wenchuan, China, earthquake and are reminiscent of the diverse slip mechanisms documented in aftershock sequences of other California earthquakes like Loma Prieta (Beroza & Zoback, 1993; Zoback & Beroza, 1993) and Northridge (Shearer et al., 2003).

For comparison with the waveform-based measure of earthquake similarity, we also examine the focal mechanism rotation of each earthquake with respect to nearby events. Overall, the results of the waveform-based and mechanism-based similarity measurements are in good agreement (Figures 2–4). We observe a step change in the distribution of focal mechanism rotations aligned with the beginning of the July 2019

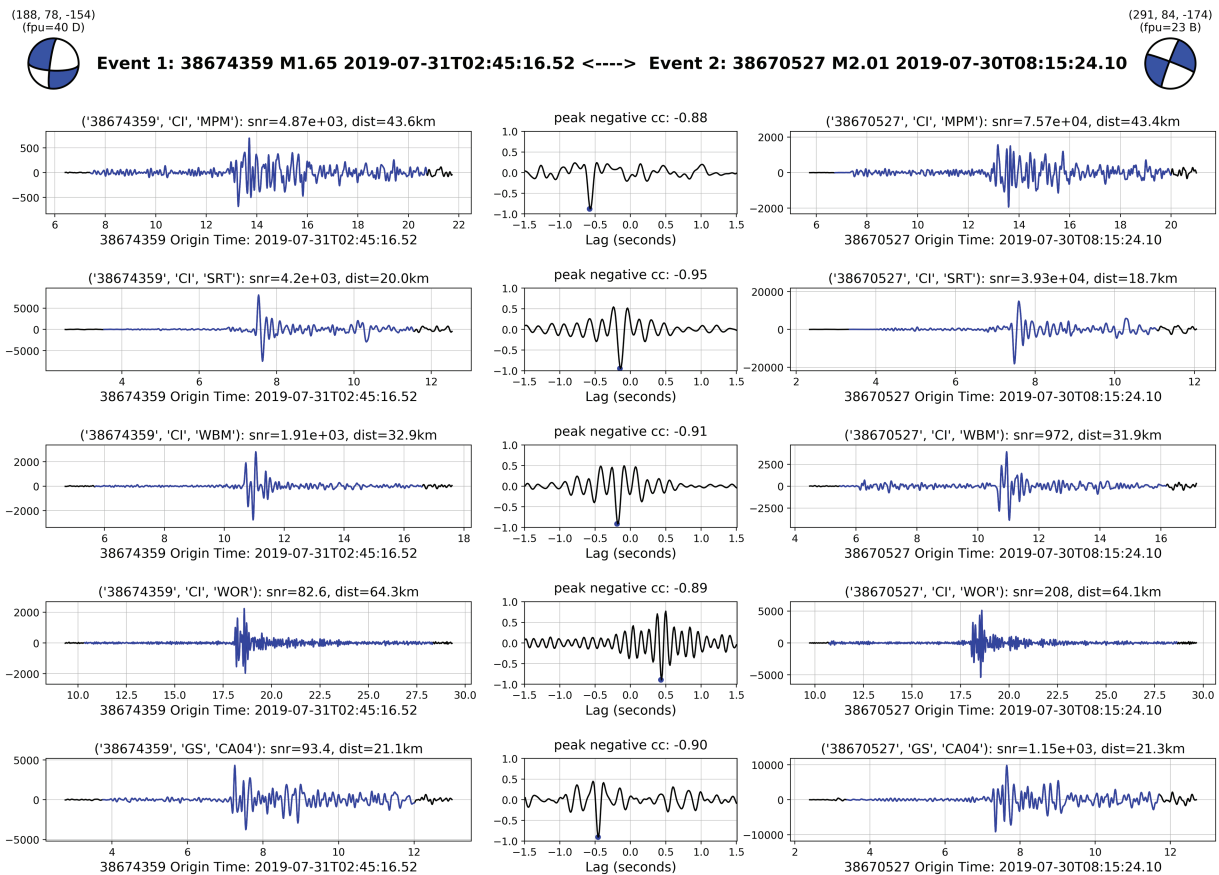


Figure 5. Example of an antisimilar earthquake pair, with waveforms shown at five common stations. The left column shows waveforms at Stations MPM, SRT, WBM, WOR, and CA04 for Event 38674359, while the right column shows waveforms at these same stations for Event 38670527. The distance-dependent cross-correlation time window for each waveform is denoted in blue. The center column shows the cross-correlation functions for these two events, which are sharply peaked at values near -1 . Focal mechanism estimates for both earthquakes are shown schematically in the upper left and right portions of the figure for reference.

sequence, along with spatial patterns that are largely consistent with those derived directly from the waveforms themselves. The mechanism-based measurements have larger uncertainties and are coarser in their spatial and temporal resolution, since reliable mechanism measurements are not routinely available for smaller earthquakes. This is a particularly important limitation to consider in the earlier years of our data set, when station coverage is sparser and network processing workflows did not as consistently attempt to compute focal mechanism at lower magnitudes. Despite this, the correspondence between our waveform and mechanism based measurements of earthquake similarity lends confidence to the results as a whole and to the application of each technique in isolation.

4. Discussion and Conclusions

In this study, we examine spatial and temporal patterns in the similarity of earthquake rupture processes near Ridgecrest, California. We show that the July 2019 Ridgecrest events directly lead to (1) a drop in median similarity as the sequence commences, (2) the emergence of coherent spatial patterns of similarity within the rupture zone, and (3) the occurrence of aftershocks with antisimilar waveforms over short length scales. We emphasize that these results are purely observational, and detailed physical modeling will be needed to explain them in full. Nevertheless, it is instructive to discuss the potential physical mechanisms driving these observations.

One way to interpret our waveform-based measurements of earthquake similarity is as a proxy for homogeneity in the local stress field. Prior to the July 2019 sequence, earthquakes in this area exhibit relatively high similarity to nearby events, indicating that they slip with similar mechanisms on closely aligned or identical faulting structures. This makes intuitive sense, as background seismicity should by definition be

well oriented for failure in the regional stress field. In the aftermath of the $M6.4$ and $M7.1$ events, the picture becomes more complicated, with nonstationary changes in stress and strength throughout the region. At first glance, it seems counterintuitive that a near-complete stress drop might produce a heterogeneous residual stress field. However, a substantial reduction in the initial pre-stress would allow post-event stress orientations to significantly vary over short length scales near the rupture plane, in direct correspondence with variability and roughness in the mainshock slip distribution. This local complexity in stress may cause earthquakes to rupture with differing slip orientations, even on a single faulting structure. Moreover, the observations of along-strike variations in earthquake similarity, and in particular the clustering of low-similarity events in the high-slip regions of the $M7.1$ rupture, supports the notion that waveform similarity lends insight into the details of the stress field at length scales of tens to hundreds of meters.

Ross et al. (2019) combined detailed analyses of seismic and geodetic datasets to image the highly complex faulting of the Ridgecrest earthquake sequence, which comprised dozens of interlocking and orthogonal structures within a compact spatial area. Ridgecrest is thus consistent with prior field observations and dynamic rupture modeling, which both demonstrate that large earthquakes can generate substantial damage networks of off-fault fractures in the region surrounding the main rupture trace (Klinger et al., 2018; Okubo et al., 2019; Thomas et al., 2017). This type of incipient faulting complexity may play an important role in the low levels of earthquake similarity that we observe during the Ridgecrest aftershock sequence, with antisimilar aftershocks being an extreme though visceral example. Earthquake pairs occurring on structures of different orientation would necessarily be less similar to one another than pairs occurring on the same structure. It is notable that the Wenchuan earthquake, where antisimilar aftershock waveforms were also observed (Ma & Wu, 2013), exhibited comparably high levels of near-field faulting complexity (Zhang et al., 2010).

Earthquake rupture processes are sensitive to changes in both stress and strength. Because of this, it difficult to separate the effects of stress-driven differences in slip directions from strength-driven differences in fault orientations using measures of waveform similarity alone, which are sensitive to their joint effect. Future work combining detailed waveform analysis with numerical modeling of earthquake rupture with off-fault damage may be key to resolving this ambiguity, as only in the latter case do we have full access to the 3-D stress and strength field. This line of research has shown some promise with focal mechanism data, albeit at coarser resolution than considered in this study. Hardebeck (2014), for example, used estimates of static and dynamic stress changes in several California earthquake sequences to show that, to within the uncertainties, preshock and aftershock events tend to occur on fault planes with similar orientations, even if their slip directions differ.

It is interesting to consider whether our observations of coherent spatial and temporal variations in earthquake similarity are feature common to most large earthquakes, or pertain only to Ridgecrest and a smaller subset of complex earthquake sequences. Liu et al. (2019), for example, provide a compelling argument that the occurrence of the Ridgecrest sequence on an immature fault system may have controlled some of its central seismological features, including the low mainshock rupture velocity and high aftershock productivity. Much of the relevant research in this field to date comes from the study of focal mechanism and stress rotations in the aftermath of large earthquakes. The literature on this subject is vast (Hardebeck & Okada, 2018), but the general consensus is that large and well-recorded earthquakes like Coalinga (Michael, 1987), Loma Prieta (Michael et al., 1990), Landers (Hauksson, 1994), Izmit (Bohnhoff et al., 2006), Denali (Ratchkovski, 2003), and Tohoku (Hardebeck, 2012) often exhibit substantial rotations in stress orientation. These observations imply that the causative faults are relatively weak and that the earthquakes in question impart near-complete stress drops. Where available, analyses of focal mechanism aftershocks for other prominent California earthquake sequences point to a diversity of faulting mechanisms (Beroza & Zoback, 1993; Shearer et al., 2003; Zoback & Beroza, 1993). Such studies are limited by the quantity and quality of focal mechanism estimates, which are relatively sparse and uncertain for smaller earthquakes. In part because of this, imaging spatial and temporal variations in the stress field remain a challenging task. Large-scale waveform-based measurements of earthquake similarity, as proposed in this study, may provide a high-resolution tool to image local complexity in the stress field and fault orientations at length scales of hundreds of meters or less. Improved observational constraints of this type will be required to advance our understanding of how earthquakes nucleate, rupture, and arrest in the years to come.

Acknowledgments

The seismic waveform, earthquake catalog, and focal mechanism data that form the basis of this study are publicly available from the Southern California Earthquake Data Center (<https://scedc.caltech.edu>). Data Set S1 in the supporting information contains the relocated earthquake catalog and results of the similarity analysis presented in this study. Our calculations use publicly available Python packages including ObsPy (Beyreuther et al., 2010) and the open source GrowClust software (<https://github.com/dttrugman/GrowClust>) for earthquake relocations. D. Trugman acknowledges institutional support from the Laboratory Directed Research and Development (LDRD) program of Los Alamos National Laboratory under Project 20180700PRD1. P. Johnson was supported by the Department of Energy (DOE) Office of Science. We are grateful to J. Vidale, an anonymous reviewer, and Editor J. Ritsema for constructive comments and suggestions that improved the manuscript. We also thank C. Hulbert, I. McBrearty, B. Rouet-Leduc, C. Ren, R. Guyer, and H. Bhat for insightful discussions while crafting and revising this work.

References

- Barnhart, W. D., Hayes, G. P., & Gold, R. D. (2019). The July 2019 Ridgecrest, California earthquake sequence: Kinematics of slip and stressing in cross-fault ruptures. *Geophysical Research Letters*, *46*, 11,859–11,867. [en. https://doi.org/10.1029/2019GL084741](https://doi.org/10.1029/2019GL084741)
- Beroza, G. C., & Zoback, M. D. (1993). Mechanism diversity of the Loma Prieta aftershocks and the mechanics of mainshock-aftershock interaction. *Science*, *259*(5092), 210–213.
- Beyreuther, M., Barsch, R., Krischer, L., Megies, T., Behr, Y., & Wassermann, J. (2010). ObsPy: A Python toolbox for seismology. *Seismological Research Letters*, *81*(3), 530–533.
- Bohnhoff, M., Grosser, H., & Dresen, G. (2006). Strain partitioning and stress rotation at the North Anatolian fault zone from aftershock focal mechanisms of the 1999 Izmit $M_w = 7.4$ earthquake. *Geophysical Journal International*, *166*(1), 373–385.
- Cochran, E. S., Li, Y.-G., Shearer, P. M., Barbot, S., Fialko, Y., & Vidale, J. E. (2009). Seismic and geodetic evidence for extensive, long-lived fault damage zones. *Geology*, *37*(4), 315–318.
- Frohlich, C., & Nakamura, Y. (2009). The physical mechanisms of deep moonquakes and intermediate-depth earthquakes: How similar and how different?. *Physics of the Earth and Planetary Interiors*, *173*(3), 365–374.
- Hardebeck, J. L. (2012). Coseismic and postseismic stress rotations due to great subduction zone earthquakes. *Geophysical Research Letters*, *39*, L21313. <https://doi.org/10.1029/2012GL053438>
- Hardebeck, J. L. (2014). The impact of static stress change, dynamic stress change, and the background stress on aftershock focal mechanisms. *Journal of Geophysical Research: Solid Earth*, *119*, 8239–8266. <https://doi.org/10.1002/2014JB011533>
- Hardebeck, J. L., & Okada, T. (2018). Temporal stress changes caused by earthquakes: A review. *Journal of Geophysical Research: Solid Earth*, *123*, 1350–1365. <https://doi.org/10.1002/2017JB014617>
- Hardebeck, J. L., & Shearer, P. M. (2003). Using S/P amplitude ratios to constrain the focal mechanisms of small earthquakes. *Bulletin of the Seismological Society of America*, *93*(6), 2434–2444.
- Hauksson, E. (1994). State of stress from focal mechanisms before and after the 1992 Landers earthquake sequence. *Bulletin of the Seismological Society of America*, *84*(3), 917–934.
- Hauksson, E., & Unruh, J. (2007). Regional tectonics of the Coso geothermal area along the intracontinental plate boundary in central eastern California: Three-dimensional Vp and Vp/Vs models, spatial-temporal seismicity patterns, and seismogenic deformation. *Journal of Geophysical Research*, *112*, B06309. <https://doi.org/10.1029/2006JB004721>
- Kagan, Y. Y. (2013). Double-couple earthquake source: Symmetry and rotation. *Geophysical Journal International*, *194*(2), 1167–1179.
- Klinger, Y., Okubo, K., Vallage, A., Champenois, J., Delorme, A., Rougier, E., et al. (2018). Earthquake damage patterns resolve complex rupture processes. *Geophysical Research Letters*, *45*, 10,279–10,287. <https://doi.org/10.1029/2018GL078842>
- Liu, C., Lay, T., Brodsky, E. E., Dascher-Cousineau, K., & Xiong, X. (2019). Co-seismic rupture process of the large 2019 Ridgecrest earthquakes from joint inversion of geodetic and seismological observations. *Geophysical Research Letters*, *46*, 11,820–11,829. <https://doi.org/10.1029/2019GL084949>
- Ma, X. J., & Wu, Z. L. (2013). 'Negative repeating doublets' in an aftershock sequence. *Earth, Planets and Space*, *65*(8), 923–927.
- Michael, A. J. (1987). Stress rotation during the Coalinga aftershock sequence. *Journal of Geophysical Research*, *92*(B8), 7963–7979.
- Michael, A. J., Ellsworth, W. L., & Oppenheimer, D. H. (1990). Coseismic stress changes induced by the 1989 Loma Prieta, California Earthquake. *Geophysical Research Letters*, *17*(9), 1441–1444.
- Mitchell, T. M., & Faulkner, D. R. (2009). The nature and origin of off-fault damage surrounding strike-slip fault zones with a wide range of displacements: A field study from the Atacama fault system, northern Chile. *Journal of Structural Geology*, *31*(8), 802–816.
- Okubo, K., Bhat, H. S., Rougier, E., Marty, S., Schubnel, A., Lei, Z., et al. (2019). Dynamics, radiation and overall energy budget of earthquake rupture with coseismic off-fault damage. *Journal of Geophysical Research: Solid Earth*, *124*, 11,771–11,801. <https://doi.org/10.1029/2019JB017304>
- Ratchkovski, N. A. (2003). Change in stress directions along the central Denali fault, Alaska after the 2002 earthquake sequence. *Geophysical Research Letters*, *30*(19), 2017. <https://doi.org/10.1029/2003GL017905>
- Ross, Z. E., Idini, B., Jia, Z., Stephenson, O. L., Zhong, M., Wang, X., et al. (2019). Hierarchical interlocked orthogonal faulting in the 2019 Ridgecrest earthquake sequence. *Science*, *366*(6463), 346–351.
- Shearer, P. M., Hardebeck, J. L., Astiz, L., & Richards-Dinger, K. B. (2003). Analysis of similar event clusters in aftershocks of the 1994 Northridge, California, earthquake. *Journal of Geophysical Research*, *108*, 2035.
- Thomas, M. Y., Bhat, H. S., & Klinger, Y. (2017). Effect of brittle off-fault damage on earthquake rupture dynamics. In M. Y. Thomas, T. M. Mitchell, & H. S. Bhat (Eds.), *Fault zone dynamic processes*. <https://doi.org/10.1002/9781119156895.ch14>
- Trugman, D. T., & Shearer, P. M. (2017). GrowClust: A hierarchical clustering algorithm for relative earthquake relocation, with application to the Spanish springs and Sheldon, Nevada, earthquake sequences. *Seismological Research Letters*, *88*(2A), 379–391.
- Yang, W., Hauksson, E., & Shearer, P. M. (2012). Computing a large refined catalog of focal mechanisms for Southern California (1981–2010): Temporal stability of the style of faulting. *Bulletin of the Seismological Society of America*, *102*(3), 1179–1194.
- Zhang, P., Wen, X., Shen, Z., & Chen, J. (2010). Oblique, high-angle, listric-reverse faulting and associated development of strain: The Wenchuan earthquake of May 12, 2008, Sichuan, China. *Annual Review of Earth and Planetary Sciences*, *38*(1), 353–382.
- Zoback, M. D., & Beroza, G. C. (1993). Evidence for near-frictionless faulting in the 1989 ($M 6.9$) Loma Prieta, California, earthquake and its aftershocks. *Geology*, *21*(2), 181–185.